Resonant photon transport through metal-insulator-metal multilayers consisting of Ag and SiO_2

Maiko Yoshida,[1] Satoshi Tomita,[1,*] Hisao Yanagi,[1] and Shinji Hayashi[2]
[1]*Graduate School of Materials Science, Nara Institute of Science and Technology (NAIST), 8916-5 Takayama, Ikoma, Nara 630-0192, Japan*
[2]*Graduate School of Engineering, Kobe University, Rokkodai 1-1, Nada, Kobe 657-8501, Japan*
(Received 1 April 2010; revised manuscript received 11 June 2010; published 9 July 2010)

We have conducted experimental and numerical studies on resonant photon transport through Ag-SiO_2-Ag multilayers with varying SiO_2 gap-layer thickness due to its application toward the development of a metamaterial superlens. Photon-transport spectra that have been measured using a double-prism system with a *p*-polarized He-Ne laser show a resonant photon tunneling (RPT) peak in the total reflection region and an additional peak in the propagating region. Calculated dispersion curves and electric field profiles reveal that the RPT peak is brought about by antisymmetrically coupled surface-plasmon polaritons (SPPs), very similar to the long-range SPPs in a single-metal film. The additional peak, however, is caused by TM guided modes with symmetrically coupled SPPs. We demonstrate that the TM_0 guided modes move continuously from the total reflecting region to the propagating region as the gap-layer thickness decreases. This will enable us to realize a device which converts evanescent waves into propagating waves of light, opening the possibility of an alternative type of hyperlens.

DOI: 10.1103/PhysRevB.82.045410 PACS number(s): 78.67.Pt, 42.25.Bs, 73.20.Mf

I. INTRODUCTION

Since a conventional lens uses propagation waves of light for imaging, the resolution of the lens is restricted by the wavelength of light. This is the so-called diffraction limit. Subwavelength imaging beyond the diffraction limit can, however, be achieved by using evanescent waves of light, which convey information of subwavelength structures that have large in-plane wave vectors. Theoretically, a slab made of a material with a negative index of refraction can carry all evanescent components of light, leading to perfect imaging.[1] Even a metal thin film with only negative permittivity for visible light, for example, silver (Ag), demonstrated the ability to transport a portion of evanescent waves of light via surface-plasmon polaritons (SPPs) at an interface of the metal and insulator.[2,3] This brings about a super-resolution in imaging, i.e., superlensing effect.

Various types of superlenses have been proposed. One of the candidates is a multilayer metamaterial consisting of metal and insulator thin layers.[4–8] It was proposed theoretically that the artificial anisotropy in the metamaterials conveys the evanescent waves that have large in-plane wave vectors over long distances using coupled SPPs, thus bringing about the superlensing effect.[6] The basic mechanism of the superlensing effect is a resonant tunneling of the evanescent waves.[9–14] Because the evanescent waves usually decay exponentially, the key point for achieving a higher resolution in a superlens depends on the transport of the evanescent waves without attenuation. In previous works, we conducted experimental and numerical studies on the transport of evanescent waves using resonant photon tunneling (RPT) via coupled SPPs in multilayer metamaterials. RPT was observed through three aluminum[15] or three Ag layers.[16] As the evanescent wave of light was tunneled up to 200 nm in these studies, a natural question arises: what is the maximum distance can we transport the evanescent waves of light through metal-insulator multilayers?

In order to answer this question, one of the simplest cases is studied in this paper. We split an Ag film into two Ag thin films and focus on the photon transport through the multilayers consisting of two Ag thin films with silicon dioxide (SiO_2) gap layers of varying thickness. In other words, the cores of our samples are metal-insulator-metal (MIM) structures with noble metal. The slot waveguide using such plasmonic MIM structures has been proposed;[17] a characteristic guided mode, also referred to as gap plasmons, have attracted a great deal of attention. Waveguide[18,19] and optical[20–23] properties of the plasmonic MIM structures have been studied intensively. Nonetheless, photon transport *through* the MIM structures is still an open question.

The purpose of this paper is to increase knowledge about resonant photon transport through the plasmonic MIM structures. This paper is organized as follows: Sec. II describes the experimental and numerical procedures. Preparation of multilayer samples consisting of Ag and SiO_2 is explained in detail. Photon-transport spectra measurements using a double-prism system based on an attenuated total reflection (ATR) measurement are also described. Calculations of transport spectra, electric field profiles, and dispersion curves are also outlined. Section III shows experimental and numerical results followed by discussion. The measured and calculated transport spectra show a peak in the total reflection region due to RPT. In addition, another peak in the propagation region is also observed for samples with large gap thicknesses. As the gap thickness increases, the additional peak moves into the total reflection region and finally merges with the RPT peak. Based on the calculated field profiles and dispersion curves, we reveal that the additional peak is caused by the TM_0 guided mode, which is characteristic of plasmonic MIM structures. We propose that this mode will be useful for a novel hyperlens. Section IV concludes this paper.

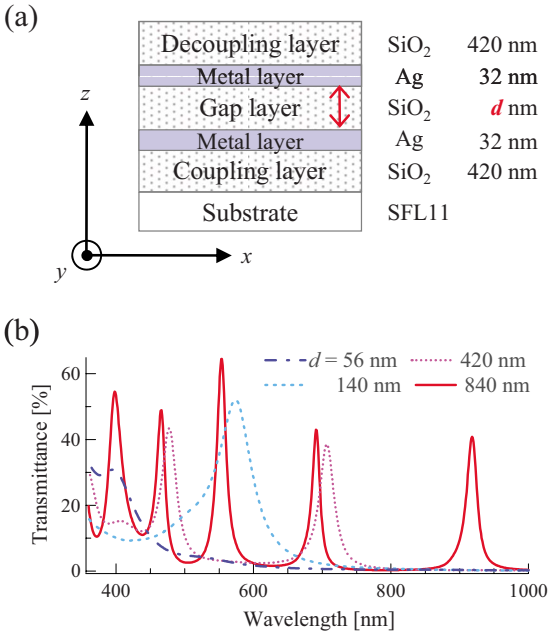

FIG. 1. (Color online) (a) The sample structure and (b) far-field transmittance of the samples measured using UV-Vis spectrometer. The dotted-dashed (blue) line, dashed (light blue) line, dotted (purple) line, and solid (red) line correspond to samples for which $d=56$ nm, 140 nm, 420 nm, and 840 nm, respectively.

II. EXPERIMENT AND CALCULATION

The multilayers were prepared using an rf-magnetron sputtering of Ag and SiO_2. The thickness of Ag and SiO_2 film was primary estimated by the sputtering duration and deposition speed, which was measured with a quartz-crystal microbalance. The thickness was then calibrated by fitting calculated light reflection spectra to measured ones at a wavelength of $\lambda=633$ nm. The fitting simultaneously brought about electric permittivity at $\lambda=633$ nm of Ag $[\epsilon_{Ag}(633)]$ and $SiO_2[\epsilon_{SiO_2}(633)]$. In this paper, we used the thickness, $\epsilon_{Ag}(633)$ and $\epsilon_{SiO_2}(633)$ determined according to the best-fitting parameters unless otherwise noted.

As shown in Fig. 1(a), we stacked an SiO_2 coupling layer (420 nm in thickness), an Ag layer (32 nm in thickness), an SiO_2 gap layer (d nm in thickness), an Ag layer (32 nm in thickness), and an SiO_2 decoupling layer (420 nm in thickness) on a high refractive index glass (SFL11) substrate. The thickness of the gap layer was changed for $d=56$, 140, 420, and 840 nm in experiments.

We measured the light reflectance and transmittance of the samples as a function of an incident angle θ_i by using a double-prism system. The double-prism system is based on an ATR measurement[9] and has been described in our previous article.[15] Briefly, a sample was sandwiched between coupling and decoupling 60° prisms made of SFL11 using index matching fluid (Diiodomethane). A bare SFL11 substrate and an SFL11 substrate with only a 250 nm SiO_2 layer were also sandwiched as reference samples for transmission and reflection, respectively. The samples with the prisms were mounted on an axis of a two-axes rotation stage. The sample was irradiated by p- or s-polarized light from a He-Ne laser ($\lambda=633$ nm) through the coupling prism at an incident angle θ_i. Reflected light at θ_i was detected using a Si photodiode, which was mounted on another axis of the stage at $2\theta_i$. Transmitted light was also detected using another Si photodiode.

Before measurements, a 100% transmission was recorded through a bare SFL11 substrate at $\theta_i=60°$. A 100% reflectance was also recorded using the substrate with 250 nm SiO_2 at $\theta_i=60°$, which is above a critical angle of the total reflection θ_c at an interface between SFL11 and SiO_2. The reflectance and transmittance of light with the multilayer sample were then measured using lock-in amplifiers. By changing θ_i, we obtained reflection and transmission spectra simultaneously. Hereinafter, the transmission spectra are called transport spectra. The reflection spectra were renormalized by the measured maximum reflectance. Additionally, we measured far-field light transmittance as a function of wavelength at a normal incidence using ultraviolet and visible (UV-Vis) spectrometer.

Reflection and transport spectra at $\lambda=633$ nm were calculated using the 2×2 transfer-matrix method. The complex permittivity of SFL11, SiO_2, and Ag was $\epsilon_{SFL11}(633)=3.161+i0$, $\epsilon_{SiO_2}(633)=2.223+i0$, and $\epsilon_{Ag}(633)=-13.203+i2.662$, respectively. $\epsilon_{Ag}(633)=-13.203+i2.662$ for calculations was obtained by the fitting of the calculated light reflection spectra to measured ones and was different from a value in a literature,[24] for example, $-15.037+i1.017$ at $\lambda=620$ nm. The difference is attributed to the surface roughness and grain boundary in the Ag layers prepared by the sputtering method. Electric field profiles in the multilayer were also calculated at a specific θ_i. Moreover, we carried out calculations of dispersion curves to reveal a normal mode in the photon transport. In dispersion calculations, we used permittivity of Ag and SiO_2 which depend on wavelength λ, $\epsilon_{Ag}(\lambda)$ and $\epsilon_{SiO_2}(\lambda)$, tabulated by Palik.[24] The permittivity of SFL11 was considered to be independent of λ and $3.161+i0$. As explained in detail in literatures,[25,26] dispersion curves can be obtained from the power dissipation spectra, which represent the power dissipated by a point dipole. We performed calculations by placing a point dipole at the center of the SiO_2 gap layer.

III. RESULTS AND DISCUSSION

A. Measured and calculated photon-transport spectra

Figure 1(b) shows far-field transmittance that was measured at a normal incidence using an unpolarized UV-Vis spectrometer of samples with varying d. The dotted-dashed (blue) line, dashed (light blue) line, dotted (purple) line, and solid (red) line correspond to samples for which $d=56$ nm, 140 nm, 420 nm, and 840 nm, respectively. We see that the number of transmission peaks increases with increasing d. The peaks are caused by multiple reflection in the multilayer. This result shows that we have succeeded in preparing multilayer samples with various d.

Reflection and transport spectra of the same samples were measured using a double-prism system. Figure 2(a) shows reflection spectra, which are so-called ATR spectra, of

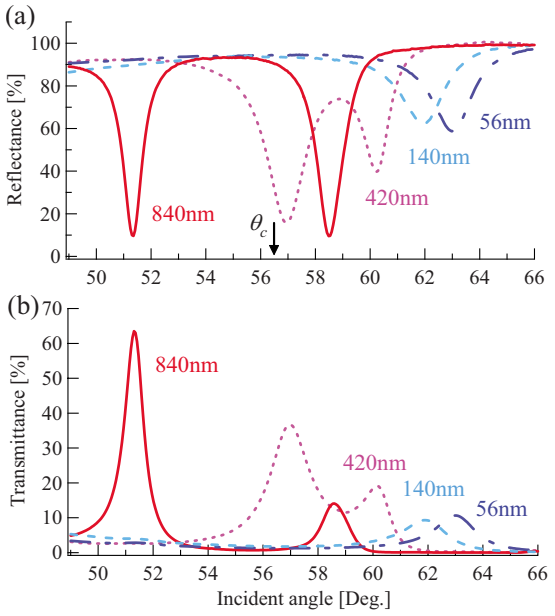

FIG. 2. (Color online) Measured (a) reflection and (b) transport spectra with p-polarized light. The dotted-dashed (blue) line, dashed (light blue) line, dotted (purple) line, and solid (red) line correspond to samples for which $d=56$ nm, 140 nm, 420 nm, and 840 nm, respectively.

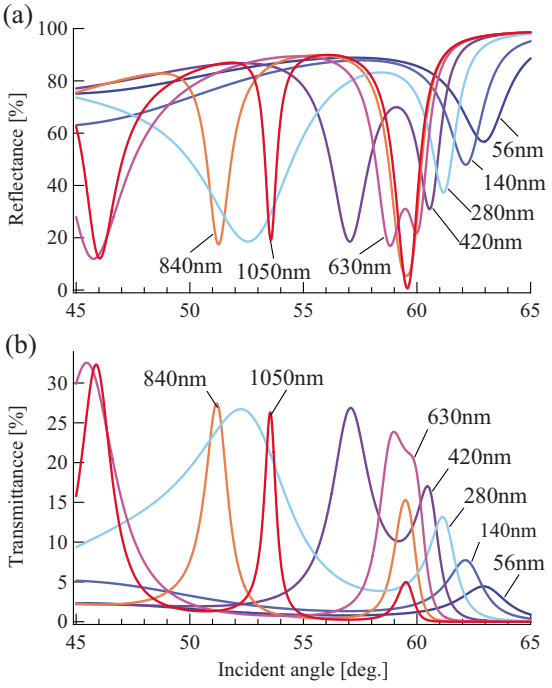

FIG. 3. (Color online) Calculated (a) reflection and (b) transport spectra with p-polarized light of $\lambda=633$ nm.

samples with various d. Figure 2(b) shows transport spectra. These spectra were obtained with p-polarized light. The arrow in Fig. 2(a) indicates $\theta_c=56.5°$. θ_c at the SFL11-SiO_2 interface is determined from the reflection measurement for a sample with only an SiO_2 film of 1260 nm in thickness on an SFL11 substrate.

For $d=56$ nm (dotted-dashed blue line) in Fig. 2(a), we see an ATR dip at about 63°, which is above θ_c. At the same position, a transport peak is observed in Fig. 2(b). Although not shown here, no dips or peaks are observed with s-polarized light. These results indicate that the dip at about 63° is caused by an excitation of SPPs at an interface of Ag and SiO_2 as the SPPs are TM waves. We see that the evanescent wave of light which has a large in-plane wave vector is resonantly tunneled via a coupled SPP.[15] The transport peak at above θ_c is thus named as an RPT peak.

With increasing d up to 140 nm (dashed light blue line), the ATR dip and RPT peak are moved to a lower angle of about 62°. When d increases to 420 nm (dotted purple line), the ATR dip and RPT peak are shifted further to 60°, which is still above θ_c. In addition, we see that a reflection dip and transport peak appeared at about 57°, which is around θ_c. For $d=840$ nm (solid red line), the ATR dip and RPT peak are reached at about 58.5°. An additional dip and peak are observed at about 51°.

Reflection and transport spectra were calculated at $\lambda=633$ nm using the 2×2 transfer-matrix method. Figure 3 shows calculated spectra with p-polarized light for $d=56$, 140, 420, and 840 nm. Spectra calculated for $d=280$, 630, and 1050 nm, which were not studied in these experiments, are also presented in the same figure. We see that the calculation reproduces the experimental results in Fig. 2: as d increases from 56 to 1050 nm, the ATR dip and RPT peak in the total reflection region above θ_c are moved to a lower angle.

In Fig. 3, calculated spectra for $d=280$ nm shows an additional broad dip and peak at about 52° below θ_c in the propagating region. Interestingly, as d increases from 280 to 630 nm, the additional dip and peak shift to a higher angle and enter into the total reflection region. They finally merge with the ATR dip and RPT peak at just above θ_c for $d=840$ nm. Another additional dip and peak at about 46° appear in a sample for which $d=630$ nm, and move to a higher angle as d increases.

Figure 4 shows polarization dependence of the spectra measured for (a) $d=420$ nm and (b) $d=840$ nm. The spectra with p-polarized light are the same as in Fig. 2. For s-polarized light in Fig. 4(a), a peak and dip appear far below θ_c. In Fig. 4(b), s-polarized light brings about two dips at about 48° and 54° and one peak at about 48° appears below θ_c. We note here that ATR dip and RPT peak in the total reflection region above θ_c are not observed with s-polarized light.

The experimental results supported by calculations reveal that, when p-polarized light is used and the gap-layer thickness d increases, the ATR dip and RPT peak at above θ_c are moved to a lower angle. More interestingly, for $d=420$ and 840 nm in experiments, additional dips and peaks are found at below θ_c. s-polarized light shows only the dips and peaks below θ_c. Calculations indicate that, with increasing d, the additional dips (peaks) shifts to a higher angle and finally merge with the ATR dip (RPT peak) at just above θ_c when the p-polarized light is used. Below, we carry out calculations of dispersion curves and electric field profiles in the multilayers, and disclose the normal modes, which cause these features in the resonant photon transport.

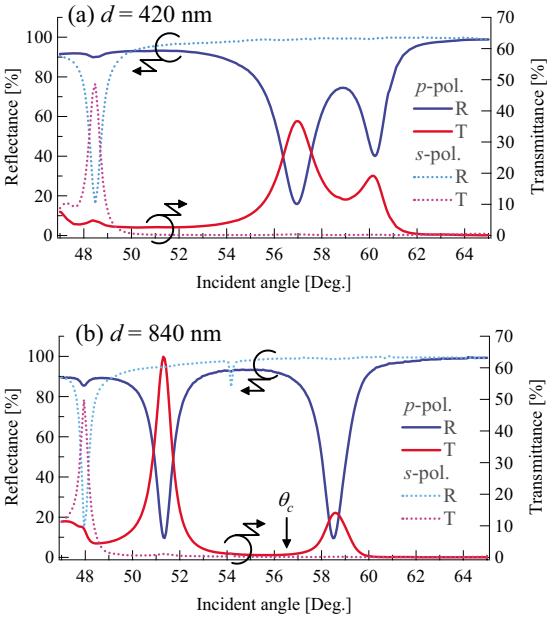

FIG. 4. (Color online) Polarization dependence of the measured spectra for (a) $d=420$ nm and (b) $d=840$ nm. Blue and light blue lines correspond to reflection spectra. Purple and red lines correspond to transport spectra. Solid lines are those obtained with *p*-polarized light. Dotted lines are those obtained with *s*-polarized light.

B. Normal modes in a sample where $d=56$ nm

Figure 5 shows calculated dispersion curves for a multilayer where $d=56$ nm. The vertical axis corresponds to photon energy. The horizontal dashed (red) line at the photon energy of 1.96 eV indicates the wavelength $\lambda=633$ nm used in the experiments. The horizontal axis represents an in-plane wave vector k_x corresponding to the incident angle θ_i in the experiments, $k_x=(2\pi/\lambda)n_p \sin\theta_i$, in which n_p is the refractive index of SFL11. The vertical dashed (red) lines indicate $k_x=0.0125$ nm^{-1}, which corresponds to an incident angle of $\theta_i=45°$ in SFL11, and $k_x=0.0160$ nm^{-1}, which corresponds to $\theta_i=65°$ in SFL11. In principle, it is theoretically possible to observe the normal modes, which intersect with the horizontal $\lambda=633$ nm line in the range of $k_x=0.0125-0.0160$ nm^{-1}. The cross point of the $\lambda=633$ nm line and SiO_2 light line (purple) corresponds to the critical

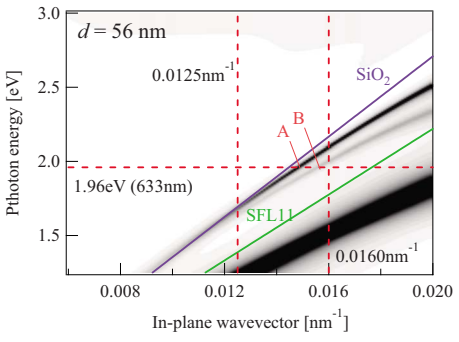

FIG. 5. (Color online) Calculated dispersion curves for $d=56$ nm.

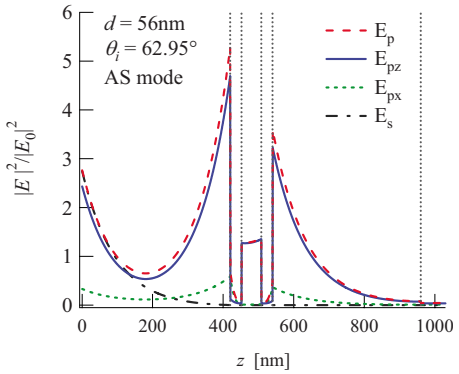

FIG. 6. (Color online) Calculated profile of electric field in the multilayer where $d=56$ nm at $\theta_i=62.95°$.

angle of total reflection θ_c, and the total reflection region is to the right side of the SiO_2 light line.

Figure 5 shows that two dispersion curves intersect with the $\lambda=633$ nm line at points A and B. We recall here that experiments and calculation results for $d=56$ nm show the ATR dip and RPT peak in the total reflection region at about 63°. The dip and peak corresponds to the point A in Fig. 5. We carried out calculation of electric field profiles at this point to disclose the nature of the normal mode represented by the dispersion curve.

Figure 6 shows an electric field profile induced in the sample by the incidence of $\lambda=633$ nm light at $\theta_i=62.95°$. The horizontal axis represents the sample structure: $z=0-420$ nm corresponds to the coupling SiO_2 layer, $z=420-452$ nm corresponds to the first Ag layer, $z=452-508$ nm corresponds to the SiO_2 gap layer, $z=508-540$ nm corresponds to the second Ag layer, and $z=540-960$ nm corresponds to the decoupling SiO_2 layer. Vertical dotted lines indicate each interface. The vertical axis is the square of the absolute value of the electric field strength normalized by the square of the incident-field intensity, $|E|^2/|E_0|^2$. E_p (dashed red line) corresponds to the electric field profile with *p* polarization and E_s (dotted-dashed black line) corresponds to that with *s* polarization. For *p* polarization, E_{pz} (solid blue line) corresponds to the electric field profile in *z* direction and E_{px} (dotted green line) corresponds to that in *x* direction.

We see that E_s is weak in the multilayers. Contrastingly, E_p is very strong at the interface between the SiO_2 coupling layer and the outer surface of the first Ag layer, and at the interface between the SiO_2 decoupling layer and the outer surface of the second Ag layer. The strong fields decay exponentially in the coupling/decoupling SiO_2 layers. These indicate that SPPs are excited at the interfaces. When we look carefully at the profile of E_{px}, the field strength in the middle of the gap layer is zero, demonstrating that the two SPPs are coupled antisymmetrically. This mode is similar to the long-range SPP mode in a single-metal film. Below, the antisymmetrically coupled mode of SPPs at the outer interface of the Ag layers is referred to as the AS mode. Figures 5 and 6 demonstrate that the AS mode causes the ATR dip and RPT peak in the total reflection region for $d=56$ nm.

Although not shown here, the calculated field profiles reveal that the other mode represented by a dispersion curve

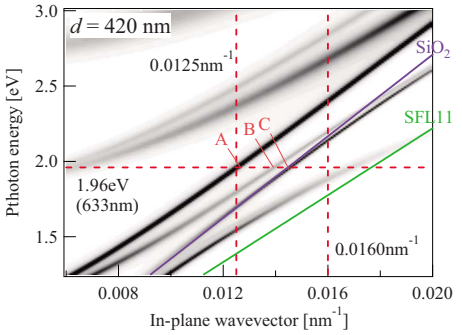

FIG. 7. (Color online) Calculated dispersion curves for $d=420$ nm.

intersecting with the $\lambda=633$ nm line at point B in Fig. 5 is determined to be a symmetrically coupled mode of SPPs at the outer interface of the Ag layers (S mode). The S mode cannot be observed in the present experiment because of the small contribution to reflection and transport spectra. In addition, the broad dispersion curve at the lower right in Fig. 5 is determined to be antisymmetrically coupled mode of SPPs at the inner interfaces of the Ag layers (MIM AS mode), also referred to as gap plasmons.[17]

C. Normal modes in a sample where $d=420$ nm

Figure 7 show dispersion curves for $d=420$ nm. The number of dispersion curves increases with d. The $\lambda=633$ nm line intersects with three dispersion curves at point A, B, and C. We recall that the measured and calculated photon-transport spectra show the RPT peak at about 60°, corresponding to point C in Fig. 7. Figure 8(a) shows the calculated electric field profile at $\theta_i=60.55°$. $z=0-420$ nm corresponds to the coupling SiO_2 layer, $z=420-452$ nm corresponds to the first Ag layer, $z=452-872$ nm corresponds to the SiO_2 gap layer, $z=872-904$ nm corresponds to the second Ag layer, and $z=904-1324$ nm corresponds to the decoupling SiO_2 layer. A profile of E_p shown in Fig. 8(a) is similar to that in Fig. 6. This indicates that the normal mode at point C is the AS mode.

We remember that experiments and calculation for $d=420$ nm show an additional dip and peak at about 57°. This corresponds to the point B in Fig. 7. Electric field profiles at $\theta_i=57.05°$ is depicted in Fig. 8(b). Figure 8(b) shows a rather different field pattern from that in Fig. 8(a). The E_p is strong at the interfaces between the inner surface of the first/second Ag layer and the SiO_2 gap layer in the MIM structure. When we look at the profile of E_{px}, the field strength is finite and nonzero, indicating that the mode is coupled symmetrically. This mode is determined to be a symmetric TM_0 guided mode, which is known as a radiative coupled SPP mode in the plasmonic MIM structures.[27] We conclude that the TM_0 mode causes the additional dip and peak in a sample where $d=420$ nm.

Calculated field profiles (not shown here) indicate that the dispersion curve crossing the horizontal $\lambda=633$ nm line at the point A corresponds to a symmetric TE_0 guided mode, which is observed with s polarization in Fig. 4(a). The dispersion curves of the TM_0 guided mode and TE_0 guided

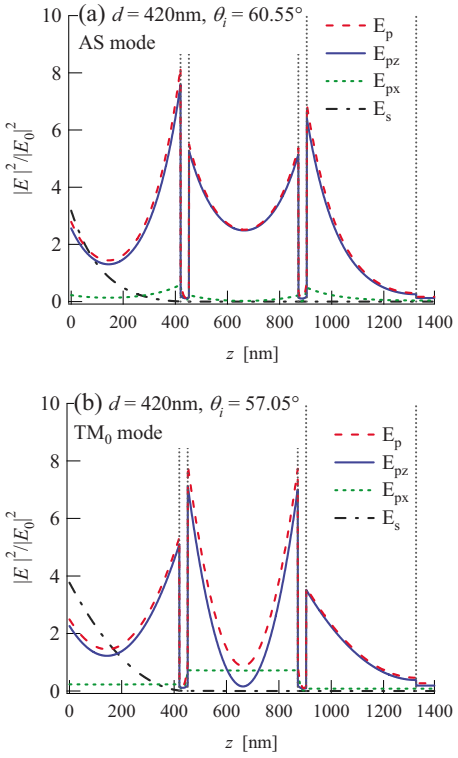

FIG. 8. (Color online) Calculated profiles of electric field in the multilayer where $d=420$ nm. (a) $\theta_i=60.55°$ and (b) $\theta_i=57.05°$.

mode in Fig. 7 are very similar to those of metal-air-metal structure (metal-clad cavity) calculated by Smith *et al.*[28]

Figure 7 shows that the dispersion curve of the TM_0 mode is approaching to that of the AS mode at a larger k_x. More importantly, the TM_0 mode crosses the SiO_2 light line and enters into the total reflection region. This causes that the dip and peak due to TM_0 is continuously moving from the propagating region to the total reflecting region as we observed in Figs 2 and 3. The seamless connection between the propagating region and the total reflecting region of the TM_0 modes in the MIM structure is very unique.

D. Normal modes in a sample where $d=840$ nm

Figure 9 shows calculated dispersion curves for a multilayer where $d=840$ nm. We see that the number of dis-

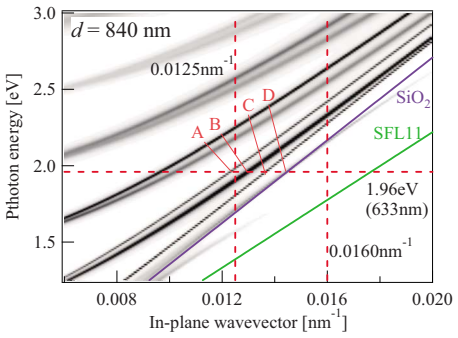

FIG. 9. (Color online) Calculated dispersion curves for $d=840$ nm.

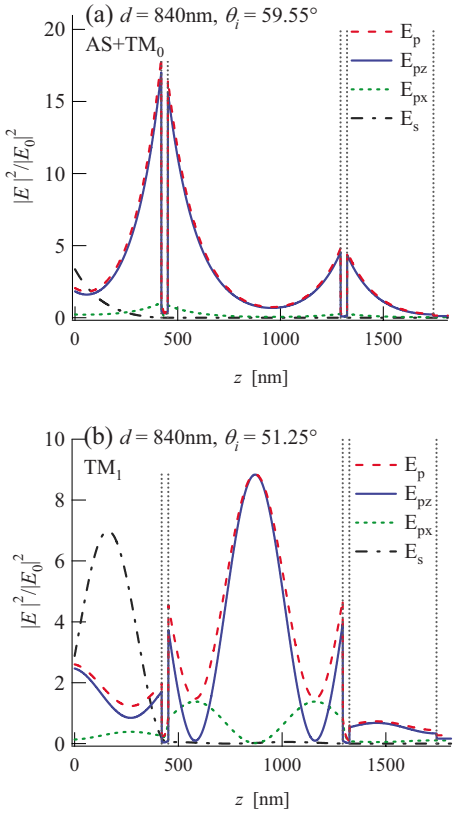

FIG. 10. (Color online) Calculated profiles of electric field in the multilayer where $d=840$ nm. (a) $\theta_i=59.55°$ and (b) $\theta_i=51.25°$.

persion curves further increases. The $\lambda=633$ nm line intersects with four dispersion curves at points A, B, C, and D. Experiments and calculation show the ATR dip and RPT peak at about 59°, corresponding to point D in Fig. 9.

Calculated electric field profiles at $\theta_i=59.55°$ are plotted in Fig. 10(a). $z=0-420$ nm corresponds to the coupling SiO_2 layer, $z=420-452$ nm to the first Ag layer, $z=452-1292$ nm to the SiO_2 gap layer, $z=1292-1324$ nm to the second Ag layer, and $z=1324-1744$ nm to the decoupling SiO_2 layer. Figure 10(a) shows a suspension-bridgelike field pattern, in which the electric field strength of the outer and inner interfaces of Ag films are comparable. This is caused by a combination of the AS mode and the TM_0 mode. The dispersion curve at point D is determined to be an AS mode merged with a TM_0 mode: the AS mode is thus renamed the AS+TM_0 mode

Figure 10(b) shows calculated electric field profiles at $\theta_i=51.25°$, which correspond to point B in Fig. 9. The E_p is strong at the interfaces between the inner interfaces of the first/second Ag layer with the SiO_2 gap layer. However, we see that the strongest E_p is obtained in the middle of the gap layer and two nodes in the SiO_2 gap layer. These features suggest that the dip and peak at $\theta_i=51.25°$ is caused by the TM_1 guided mode. The calculated field profiles (not shown here) suggest that the normal modes at point C and A are, respectively, determined to be TE_0 and TE_1, which are excited using *s*-polarized light in Fig. 4. We should mention the MIM AS mode and S mode in this sample. The light dispersion curve below the SiO_2 light line corresponds to the MIM AS mode. The S mode has disappeared in this sample because the gap layer is too thick.

The experimental and numerical results show that a tunneling light is obtained even though the gap layer is thicker than the incidence wavelength. This enables us to carry the evanescent wave of light for a long distance. A sample with $d=420$ nm shows the highest intensity of the RPT peak in this experiments (Fig. 2). Simulation results shown in Fig. 3 indicates that the highest intensity of the RPT peak is achieved just before the merging of the AS mode with the TM_0 mode. From this point of view, the TM_0 mode is a drawback for long-distance transport of the near-field light. Nevertheless, the TM_0 modes offer another opportunity to apply the MIM structures to a hyperlens[29] in which the evanescent waves are converted to the propagating waves.

Implementations of the hyperlens have already been reported. Liu *et al.*[30] demonstrated a far-field optical superlens, which is composed of an Ag slab having periodic corrugations fabricated by electron-beam lithography. Smolyaninov *et al.*[31] showed a magnifying superlens consisting of concentric rings of resin deposited on a gold film surface. An optical hyperlens consisting of a curved periodic stack of Ag and insulating thin films deposited on a half-cylindrical cavity fabricated on a quartz substrate is also demonstrated.[32] In comparison with these implementations, the plasmonic MIM structures require uncomplicated preparation scheme. If we prepare an MIM structure in which the gap-layer thickness is changed gradually, the TM_0 modes can be moved from the total reflection region to the propagating region. This will enable us a conversion of the evanescent waves to the propagating waves of light, opening a way to realize a simple type of hyperlens by using the MIM structure with a wedgelike gap layer.

The TM_0 modes in the plasmonic MIM structures are caused by symmetrically coupled SPPs at inner interfaces of Ag films. Nevertheless, electric field profiles of the TM_0 modes look similar to the guided mode as shown in Figs. 8 and 10. We think that this discrepancy is the origin of the seamless connection between the propagating region and the total reflecting region as shown in Figs. 7 and 9 of the TM_0 guided modes, which is the unique feature of the plasmonic MIM structures.

IV. CONCLUSION

Resonant photon transport in metal-insulator-metal multilayers consisting of Ag and SiO_2 has been studied. The reflection and transport spectra were measured using a double-prism system. The transport spectra with *p*-polarized light showed a peak in the total reflection region due to RPT. In addition, another peak in the propagation region was observed in samples with large gap-layer thickness. As the gap-layer thickness increased, the additional peaks moved into the total reflection region and finally merged with the RPT peak. The intensity of RPT peak was maximized just before the mergence. Based on the calculated dispersion curves and field profile, our investigation reveals that the RPT peak is

caused by the antisymmetrically coupled SPP mode at outer interfaces of Ag layers and that the additional peaks are caused by the TM guided modes, which arise from a symmetric coupling of SPPs at inner interfaces of Ag layers. The TM_0 modes provide a continuous connection between the propagating region and the total reflecting region. This suggests that a possible application of plasmonic MIM structures will be a novel type of hyperlens, which converts evanescent waves to propagating waves of light.

ACKNOWLEDGMENTS

The authors acknowledge M. Matsunaga for his contribution in the initial stage of this work. A part of this work was supported by MEXT KAKENHI (Grant No. 19710081).

*tomita@ms.naist.jp

[1] J. B. Pendry, Phys. Rev. Lett. **85**, 3966 (2000).
[2] N. Fang, H. Lee, C. Sun, and X. Zhang, Science **308**, 534 (2005).
[3] D. O. S. Melville and R. J. Blaikie, Opt. Express **13**, 2127 (2005).
[4] S. A. Ramakrishna, J. B. Pendry, M. C. K. Wiltshire, and W. J. Stewart, J. Mod. Opt. **50**, 1419 (2003).
[5] P. A. Belov and Y. Hao, Phys. Rev. B **73**, 113110 (2006).
[6] B. Wood, J. B. Pendry, and D. P. Tsai, Phys. Rev. B **74**, 115116 (2006).
[7] D. O. S. Melville and R. J. Blaikie, J. Opt. Soc. Am. B **23**, 461 (2006).
[8] M. J. Roberts, A. Guenthner, and S. Feng, Opt. Express **15**, 11999 (2007).
[9] R. Dragila, B. Luther-Davies, and S. Vukovic, Phys. Rev. Lett. **55**, 1117 (1985).
[10] S. Hayashi, H. Kurokawa, and H. Oga, Opt. Rev. **6**, 204 (1999).
[11] I. Avrutsky, Y. Zhao, and V. Kochergin, Opt. Lett. **25**, 595 (2000).
[12] S. A. Darmanyan and A. V. Zayats, Phys. Rev. B **67**, 035424 (2003).
[13] L. Lin, R. J. Reeves, and R. J. Blaikie, Phys. Rev. B **74**, 155407 (2006).
[14] I. R. Hooper, T. W. Preist, and J. R. Sambles, Phys. Rev. Lett. **97**, 053902 (2006).
[15] S. Tomita, T. Yokoyama, H. Yanagi, B. Wood, J. B. Pendly, M. Fujii, and S. Hayashi, Opt. Express **16**, 9942 (2008).
[16] M. Matsunaga, S. Tomita, T. Yokoyama, and H. Yanagi, Proc. SPIE **7395**, 73951J (2009).
[17] J. A. Dionne, L. A. Sweatlock, H. A. Atwater, and A. Polman, Phys. Rev. B **73**, 035407 (2006).
[18] F. Kusunoki, T. Yotsuya, and J. Takahara, Opt. Express **14**, 5651 (2006).
[19] M. J. Preiner, K. T. Shimizu, J. S. White, and N. A. Melosh, Appl. Phys. Lett. **92**, 113109 (2008).
[20] F. Intravaia and A. Lambrecht, Phys. Rev. Lett. **94**, 110404 (2005).
[21] H. T. Miyazaki and Y. Kurokawa, Phys. Rev. Lett. **96**, 097401 (2006).
[22] H. J. Lezec, J. A. Dionne, and H. A. Atwater, Science **316**, 430 (2007).
[23] J. Feng, T. Okamoto, J. Simonen, and S. Kawata, Appl. Phys. Lett. **90**, 081106 (2007).
[24] E. D. Palik, *Handbook of Optical Constants of Solids* (Academic Press, New York, 1997).
[25] W. L. Barnes, J. Mod. Opt. **45**, 661 (1998).
[26] W. L. Barnes, J. Lightwave Technol. **17**, 2170 (1999).
[27] E. N. Economou, Phys. Rev. **182**, 539 (1969).
[28] L. H. Smith, M. C. Taylor, I. R. Hooper, and W. L. Barnes, J. Mod. Opt. **55**, 2929 (2008).
[29] Z. Jacob, L. Alekseyev, and E. Narimanov, Opt. Express **14**, 8247 (2006).
[30] Z. Liu, S. Durant, H. Lee, Y. Pikus, N. Fang, Y. Xiong, C. Sun, and X. Zhang, Nano Lett. **7**, 403 (2007).
[31] I. I. Smolyaninov, Y.-J. Hung, and C. C. Davis, Science **315**, 1699 (2007).
[32] Z. Liu, H. Lee, Y. Xiong, C. Sun, and X. Zhang, Science **315**, 1686 (2007).